Performance analysis of CO2 thermal management system for electric vehicles in winter

Published Version:
Wang, H., Song, Y., Valdiserri, P., Rossi di Schio, E., Yang, X., Wang, X., et al. (2024). Performance analysis of CO2 thermal management system for electric vehicles in winter. APPLIED THERMAL ENGINEERING, 236, 1-12 [10.1016/j.applthermaleng.2023.121700].

Availability:
This version is available at: https://hdl.handle.net/11585/946115 since: 2023-10-24

Published:
DOI: http://doi.org/10.1016/j.applthermaleng.2023.121700

Performance analysis of CO_2 thermal management system for electric vehicles in winter

Haidan Wang[a,b], Yulong Song[a], Paolo Valdiserri [b], Eugenia Rossi di Schio [b], Xu Yang [a*] Xixi Wang[c]

Feng Cao[a*]

[a] School of Energy and Power Engineering, Xi'an Jiaotong University, Xi'an 710049, China

[b] Department of Industrial Engineering, University of Bologna, Bologna, Italy

[c] Yutong Bus Co., Ltd., Zhengzhou, China

[*]Corresponding author, Email: fcao@mail.xjtu.edu.cn (Feng Cao); yangzx@mail.xjtu.edu.cn (Xu Yang);

Tel: 86-029-82663583;

Fax: 86-029-82663583

Abstract

CO_2 is well-suited for thermal management systems (TMSs) in electric vehicles, particularly in winter when both the cabin air and the battery require heating. However, due to the distinct heat exchange boundary conditions of these two heated components, traditional theories of optimal operation of CO_2 cycle are not applicable. In this paper, the system characteristics of a CO_2 TMS in the cabin-and-battery mixed heating mode are comprehensively investigated. The results show that there is a pseudo-optimal discharge pressure that maximizes the COP_{TMS}, regardless of whether the system is operating in a transcritical or subcritical mode. In addition, besides the global optimal COP_{TMS}, there may still be other local maximum points, which are determined by the CO_2 flow distribution in both gas coolers and the COP rise rate of the battery cycle. Furthermore, this work offers a thorough investigation of the impact of essential factors on the pseudo-optimal discharge pressure and proposes an accurate prediction approach for the best control of the CO_2 TMS. The CO_2 TMS can still ensure a COP_{TMS} above 2.0 to meet the thermal demands of both the cabin and the battery even under the challenging operating circumstances of -20 °C, proving the technology's great

competitiveness.

Keywords

Transcritical CO_2 system, Heat pump technology, Thermal management system, Optimal performance, Electric vehicles.

Nomenclature			
A	Area, (m^2)	TMS	Thermal management system
C_d	discharge coefficient		
c_p	Specific heat capacity, (kJ/(kg·K))	**Greek symbols**	
h	Enthalpy, (kJ/kg)	α	Heat transfer coefficient, (W/(m^2·K))
L_{vap}	latent vaporization heat of water, (kW/kg)	ε	Pressure ratio of compressor
$\dot{m}_{cond}$	condensate mass flow rate, (kg/s)	η_e	Compressor motor efficiency
$\dot{m}_{CO_2}$	mass flow rate of CO_2, (kg/s)	η_{is}	Compressor isentropic efficiency
N	The number of segments of heat exchanger	η_V	The ratio of the theoretical volume of the expander to the compressor
$\dot{N}_{com}$	Speed of compressor, (RPM)	ρ	Density, (kg/m^3)
P	Pressure, (bar）		
$\dot{Q}$	Heat flow, (W)	**Subscripts**	
T	Temperature, (℃)	a	Ambient
$\dot{V}$	Coolant flow rates, (L/min)	air	Air
V_d	Displacement, (m^3)	bat	Battery heating cycle
$\dot{W}$	Power consumption, (W)	cab	Cabin air heating cycle
		c	Coolant
abbreviations		com	Compressor
AC	Air conditioning	dis	Discharge of Compressor
BTMS	Battery thermal management system	EEV	Electronic expansion valve
COP	Coefficient of performance	j	Index of each segment
EEV	Electronic expansion valve	in	Inlet
EV	Electric vehicle	opt	Optimal
HP	Heat pump	out	Outlet
HX	Heat exchanger	pse-opt	Pseudo-optimal
HVAC	Heating, ventilation and air	suc	Suction of the compressor

	conditioning		
IHX	Internal heat exchanger	TMS	Thermal management system
PTC	Positive temperature coefficient	wall	Tube wall of heat exchangers

1 Introduction

Traditional internal combustion engine vehicles are gradually being replaced with electric vehicles (EVs) as a result of the global energy crisis and air pollution [1]. Rechargeable lithium-ion batteries have become the primary source of power for EVs due to their high specific power, long cycle life, and high specific energy density [2]. With an ideal operating temperature range of 10 °C to 50 °C, lithium-ion batteries are quite sensitive to ambient temperature [3]. The temperature differential between the cell should be smaller than 5 °C to increase service life [4]. At low temperatures, lithium-ion batteries lose a significant amount of their capacity and power density. In recent years, as batteries' size and capacity have increased, air-cooled battery thermal management systems (BTMS) have hardly been able to keep up [5]. Liquid cooling, however, can improve battery performance at high rate of charge and discharge [6]. The liquid cooling BTMS can be more suitable for EVs.

In order to keep the passengers comfortable, the cabin air must be either cooled or heated in addition to meeting the needs of the battery [8]. Since there is no internal combustion engine in EVs that can generate enough waste heat [9], and the use of a positive temperature coefficient heater can significantly compromise the cruising range [10], the integrated air conditioning (AC)/ heat pump (HP) system is an energy-saving way to meet passengers comfort requirements [11-13]. In addition, the heating and cooling needs of the battery can be met by using the integrated AC/HP system by adding heat exchangers and parallel valves [14-15].

Park et al. [16] created a numerical model of refrigerant-based BTMS. The findings indicated that refrigerant temperature was more closely connected to battery temperature than refrigerant mass flow rate. According to Cen and Jiang [17], an EV battery pack's thermal performance can be significantly improved by a battery cooling system that is connected to the main AC system via an additional expansion valve. Comprehensive research was done on the BTMS performance by Tang et al. [18]. The findings revealed that if the compressor speed is greater than 4000 rpm, the battery inlet coolant temperature can remain below 25 °C even when the surrounding temperature is above 40 °C. Shen and Gao [19] created a simulation model for the refrigerant-based BTMS and discovered that it can effectively reduce the battery temperature rise (≈25 °C). Even in high-temperature and high-speed settings, it is possible to guarantee the temperature consistency across battery cells to within 3 °C. Tian et al. [20] proposed TMS for battery cooling, motor cooling, and cabin thermal comfort. With motor waste heat recovery, the coefficient of performance (COP) was raised to 25.55%. TMS heaters increased a vehicle's operating range by 31.71% when compared to PTC heaters. A TMS based on refrigerants was proposed by Guo and Jiang [21]. They showed that the suggested TMS, which has both a cabin-and-battery mixed cooling mode as well as a cabin-and-battery mixed heating mode, can successfully control both the cabin's air temperature and the battery pack's temperature.

It is worth noting that the above studies all use R134a as the refrigerant, which has a GWP of 1430 and is about to be replaced [22]. Carbon dioxide, as an environmentally friendly refrigerant, has now received attention in the field of automotive air conditioning. In particular, the excellent heating performance of CO_2 systems in winter has the potential to solve the problem of mileage anxiety caused by winter heating [23-25]. In addition, when the outlet temperature of the gas cooler is higher than 30 °C, there is an optimal discharge pressure in the supercritical zone due to the gradient properties of the isotherms to maximize the COP [26]. However, Wang et al. [27] demonstrated that there exists an optimal discharge pressure to be controlled in subcritical conditions due to the heat transfer capacity limitation of the gas cooler in winter conditions. This particular optimal discharge pressure is denoted as the pseudo-optimal discharge pressure ($P_{pes\text{-}opt}$).

Yin et al. [28] proposed a novel CO_2 system with battery evaporative cooling to deal with the potential thermal runaway problem due to the control instabilities of two-phase evaporative cooling. The cooling characteristics of a transcritical CO_2 TMS were studied by Wang et al. [29] They revealed the effects of CO_2 evaporation temperature and vapor quality on stable optimal discharge pressure control.

Although plentiful excellent researches have been carried out, more research is still needed on the CO_2 thermal management systems used in EVs, particularly in winter heat pump conditions where both the battery and cabin must be heated simultaneously. In this paper, a liquid-cooled CO_2 thermal management system test rig and simulation models were analyzed to close the research gap. Additionally, numerous PI controllers and a cabin thermal model were combined to fully analyze the winter performance of the CO_2 liquid-cooled thermal management system. Furthermore, we demonstrate that there exists a global pseudo-optimal discharge pressure in the cabin-and-battery mixed heating mode regardless of the system state of subcritical or transcritical cycles. In addition to the global optimal value, other local maximum points may still exist. To accurately predict the optimal performance to be attained by the TMS, it is then investigated how variable parameters such as ambient temperature, battery thermal demand (including chiller inlet coolant temperature and coolant flow rate), and passenger compartment fresh air ratio (i.e., HVAC inlet air temperature) affect the $P_{pes\text{-}opt}$ value. Finally, a $P_{pse\text{-}opt}$ prediction equation is proposed for maximizing the performance of CO_2 thermal management system in cabin-and-battery mixed heating mode for winter. It presents a solution for the optimal control of the CO_2 thermal management system. Maximum energy efficiency could be achieved with this research, which will also increase the driving range of EVs.

2 System description and modeling details

2.1 System description

Fig. 1. displays the schematic diagram of the CO_2 thermal management system that can jointly heat the cabin air and the battery. The compressor compresses the CO_2 fluid into a high-temperature, high-pressure superheated vapor, which is then split into two streams. One path goes via the electronic expansion valve (EEV) 1 to become a

low-temperature, low-pressure fluid after flowing into the indoor heat exchanger (HX) to warm the cabin. The other path enters the chiller where the battery is heated (A 50% aqueous solution of ethylene glycol is used to heat the battery after absorbing heat in the chiller). The CO_2 fluid changes into a low-temperature, low-pressure fluid as it passes through the EEV 2. The combined fluid from the two paths passes through the internal heat exchanger (IHX) before entering the outdoor HX for evaporation. Saturated vapor from the accumulator travels back to the compressor through the IHX. In this mode, the IHX does not work because it performs the heat exchange of the low-pressure two-phase fluid and the saturated vapor. IHX performs effectively only in the cooling mode [12]. Fig.2. shows the lgP-h diagram of the system. In addition, 4 PI controllers are designed to ensure the smooth operation of the system:

1) The temperature of the air sent into the cabin was set at 42 ºC by adjusting the speed of the compressor;
2) The temperature of the cabin air was set at 20 ºC by adjusting the speed of the indoor fan;
3) The discharge pressure of the compressor was adjusted by adjusting the flow area of EEV 1;
4) A 2 ºC coolant temperature gradient between the inlet and outlet of the chiller was achieved by adjusting the EEV 2, ensuring uniform battery cell temperature.

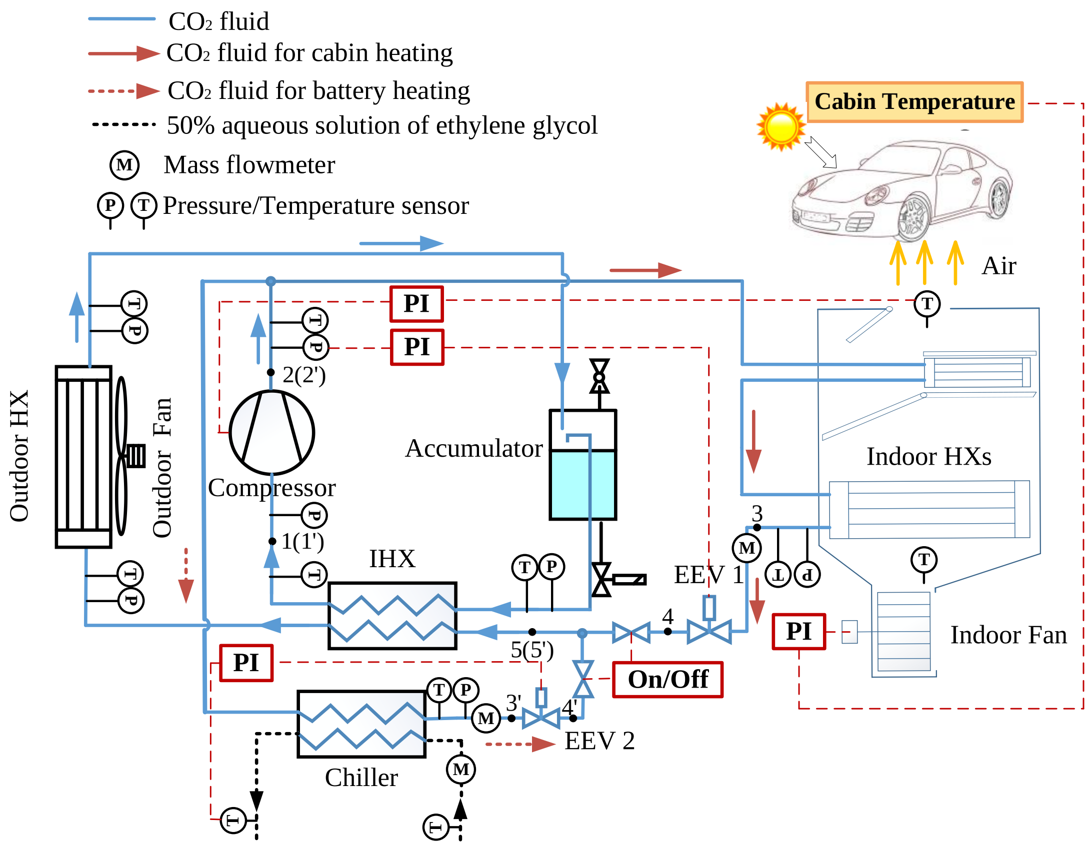

Fig.1. The schematic diagram of the CO_2 TMS.

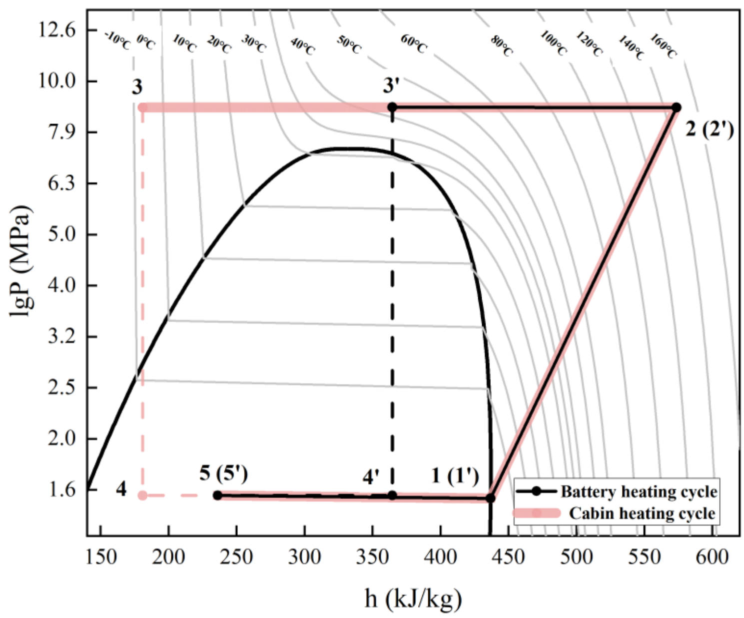

Fig.2. The lgP-h diagram of the heating cycle.

2.2 modeling details

In this study, the GT-SUITE is used as a platform to build a complete CO_2 thermal management system according to a rationally designed experimental rig. A cabin model as well as PI controllers were added to investigate the performance of the TMS in winter. GT-SUITE is a comprehensive system simulation software that encompasses multiple physical domains involving 1D and 3D simulations. It covers various physical fields such as fluid dynamics, heat transfer, mechanics, electrochemistry, and more. GT-SUITE is widely used for simulation work in thermodynamics-related domains [30-32] and vehicles [33].

2.2.1 Heat exchanger models

All heat exchangers are based on the *HxMaster and HxSlave* models. The *HxMaster* template is used to model heat transfer between the fluid on one side of a heat exchanger and the wall of the heat exchanger. Most characteristics of the heat exchanger (the detailed structure, materials, weight, and heat transfer correlations of the heat exchanger et.al) are entered in the *HxMaster* template, and the slave part is generally only of interest to declare initial conditions. The heat exchanger models are constructed using the moving boundary method.

Table 1

The modeling specifics of components.

Equipment	Specification

Indoor HXs and Outdoor HX	Type: microchannel finned tube Indoor HXs: 210 mm (length) × 190 mm (height) × 14 mm (width) 230 mm (length) × 230 mm (height) ×14 mm (width) Outdoor HX: 660 mm (length) × 515 mm (height) × 16 mm (width)	$\dot{Q}_{CO_2,air} = \sum_{j=1}^{N}(\eta_{fin}\alpha_{j,air,wall}A_j(T_{wall,j} - T_{air,j}) + \dot{m}_{cond,j} \cdot L_{vap}$ $= \sum_{j=1}^{N}\alpha_{j,CO_2,wall}A_j(T_{CO_2,j} - T_{wall,j})$
IHX	Type: concentric tube Length: 1600 mm Inside diameter: 16mm Outside diameter: 22mm	$\dot{Q}_{CO_2,CO_2} = \sum_{j=1}^{N}\alpha_{j,CO_2,CO_2}A_j(T_{CO_2,j,1} - T_{CO_2 j,2})$ $\alpha_{j,CO_2,CO_2} = \left(\frac{1}{\alpha_{CO_2,j,1}} + \frac{1}{\alpha_{CO_2,j,2}}\right)^{-1}$
Chiller	Type: Plate heat exchanger 190 mm × 76 mm 15 plates	$\dot{Q}_{CO_2,coolant} = \sum_{j=1}^{N}\alpha_{j,CO_2,coolant}A_j(T_{CO_2,j} - T_{coolant,j})$ $\alpha_{j,CO_2,coolant} = \left(\frac{1}{\alpha_{CO_2,j}} + \frac{1}{\alpha_{coolant,j}}\right)^{-1}$

Where $\dot{Q}_{CO_2,air}$ refers to the heat exchange rate between carbon dioxide and air, kW; N is the number of segments of heat exchanger; j is the index of each segment; η_{fin} is the finned surface efficiency; α_j is the heat transfer coefficient, kW/(m^2·K); A_j is the surface areas, m^2; L_{vap} is the latent vaporization heat of water, kW/kg; $\dot{m}_{cond}$ is the condensate mass flow rate, kg/s; The subscript "wall" designates the heat exchanger's tube wall; $\dot{Q}_{CO_2,CO_2}$ refers to the heat exchange rate between two streams of CO_2 fluid (stream 1 and 2), kW; $\dot{Q}_{CO_2,coolant}$ refers to the heat exchange rate between CO_2 and 50% aqueous solution of ethylene glycol, kW.

The heat transfer coefficient, α_j, for CO_2 is determined using correlations from various researchers: Dittus-Boelter's work is employed for both single-phase liquid and single-phase vapor conditions [34]; Tang's correlations are applied for two-phase condensation [35]; Gungor's findings serve for two-phase evaporation [36]; and Yoon's research provides guidance for single-phase supercritical conditions [37]. For air, α_j is evaluated using correlations presented by Chang and Wang [38], while the α_j for the coolant is calculated using the correlations presented by Dittus-Boelter [34]. Moreover, the pressure drop can be evaluated using the equations suggested by Cruz, Coelho & Alves for Reynolds numbers below 2000 [39], and by Trinh for Reynolds numbers exceeding 4000 [40]. In cases of transition regime, the friction factor calculation employs linear interpolation between laminar and turbulent values according to the given Reynolds number.

2.2.2 Compressor model

The compressor is a rolling rotor compressor with a capacity of 8.2cc. It is modelled using the *CompPosDispRefrig* and *SpeedBoundaryRot* models. *SpeedBoundaryRot* prescribes a constant or variable angular velocity on 1-D rotational parts, it can be used to simulate a self-powered generic device. The *CompPosDispRefrig* template represents a positive displacement, volumetric efficiency based compressor. The outputs of this template are mass flow rate and enthalpy change. The mass flow rate and power consumption are calculated as Eq. (1) and Eq. (2) [41].

$$\dot{m}_{CO_2} = V_d \cdot \dot{N}_{com} \cdot \rho_{suc} \cdot \eta_v\left(\varepsilon, \dot{N}_{com}, T_{suc}\right) \tag{1}$$

$$\dot{W}_{com} = \dot{m}_{CO_2} \cdot \frac{h_{dis} - h_s}{\eta_{is}(\varepsilon, \dot{N}_{com}, T_{suc})} \cdot \frac{1}{\eta_e(\varepsilon)} \tag{2}$$

The data map for isentropic efficiency (η_{is}), volumetric efficiency (η_v) and motor efficiency (η_e) are derived from experimental data. These three parameters are jointly determined by the compressor speed ($\dot{N}_{com}$), pressure ratio (ε) and compressor suction temperature (T_{suc}). V_d is the displacement of the compressor, m^3; ρ_{suc} refers to the suction density, kg/m^3; h_s represents the enthalpy CO_2 at the suction state of the compressor, kJ/kg.

2.2.3 EEV model

The throttle valves in this study used the *OrificeConn* model. This template models an orifice, defined by diameter or area and discharge coefficients, which calculates the mass flow rate between the adjacent flow volumes. The equation, as shown in Eq. (3), is solved to calculate the flow rate through the orifice [42-43].

$$\dot{m}_{CO_2} = C_d \cdot A_{EEV} \cdot \sqrt{\frac{2\Delta P \cdot \rho_{EEV,in}}{k_{dp}}} \tag{3}$$

Where C_d is discharge coefficient, and A_{EEV} represents the circulation cross-sectional area of the EEV, m^2;

2.2.4 Other models

The car cabin volume of 3.5 m^3 has been considered. The cabin's targeted temperature is 20 °C, and the model's specifications are mentioned in [12]. The accumulator with a capacity of 1.1 L is modeled by *AccumulatorRefrig*. The *Fan* module is used to simulate indoor/outdoor fans, and the efficiency information is taken from the map that the manufacturer supplies. *PID controllers* are also used to adjust the speed of the compressor and the indoor fan in addition to the areas of the two throttle valves.

2.3 Verification of simulation models

A test rig consistent with the model has been constructed, and a series of experiments are conducted to validate the accuracy of the model. The dimensions of all components are outlined in section 2.2. A photograph of the experimental setup is presented in Fig. 3. Additionally, all temperature, pressure, and flowrate sensors installed on the test rig are shown in Fig. 1. The details of the measurement equipment and associated errors are presented in Table 2. Notably, the experimental setup excludes the cabin and the PID controller used to regulate cabin temperature, instead opting to adjust the heat supply by directly varying the airflow.

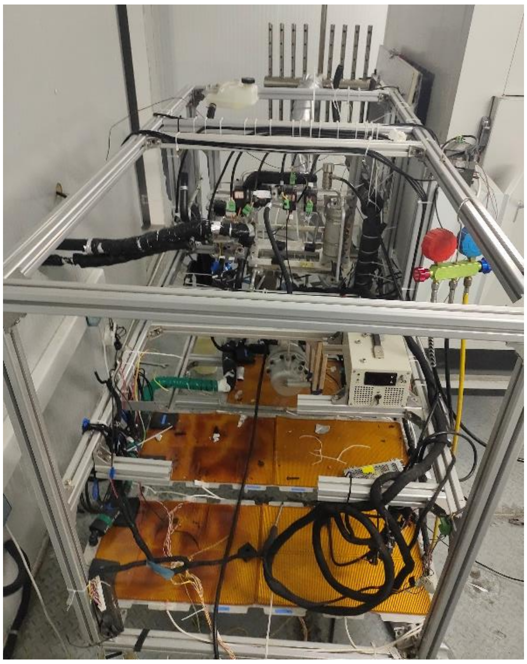

Fig.3. The photo of test rig.

Table 2

The parameters experimental measurement devices, and uncertainties.

Parameter	Component	Range and uncertainties
Air wet/dry bulb temperature	PT100 thermoelectrical resistance	-50~200 ℃, ± (0.15 + 0.0002 × reading) ℃
Coolant temperature	PT100 thermoelectrical resistance	-50~200 ℃, ± (0.15 + 0.0002 × reading) ℃
CO_2 fluid temperature	K-type thermocouple	-50~200 ℃, ±0.5 ℃
Pressure	MPM489 transmitter	0~20 MPa, 2.5 ‰ of the range
Power	WT500	15~1000 V and 0.5~40 A, ± 0.1% of reading + 0.1% of the range.
CO_2 Mass flow rate	Micro Motion Mass flowmeter	11500 $kg\cdot h^{-1}$, ±1%
Coolant Mass flow rate	Turbine flowmeter	0.2~1.2m^3/h, ±0.5%

Two distinct chambers with differing enthalpy levels are employed for multiple steady-state experiments. Each enthalpy difference chamber possesses independent control over the immediate environment's temperature and humidity. Table 3 showcases the experimental test conditions.

Table 3

Detailed parameters of operation conditions.

Parameter	Values
Amebient temperature (℃)	-20, -10, 0, 7
Indoor HX inlet air temperature (℃)	-20, -10, 0, 20
Air flow rate (m^3/h)	150,200,250,300
Coolant flow rate (L/min)	2,6,10

The error propagation for the cooling capacity was calculated using the Kline and McClintock [44] method. The largest uncertainty of the heating capacity was 3.83%. The simulation work was constructed to replicate the real-world conditions of the steady-state experiments. All the data's deviations for power consumption and heating capacity were within 6%, as displayed in Fig. 4, proving the validity of the simulation model.

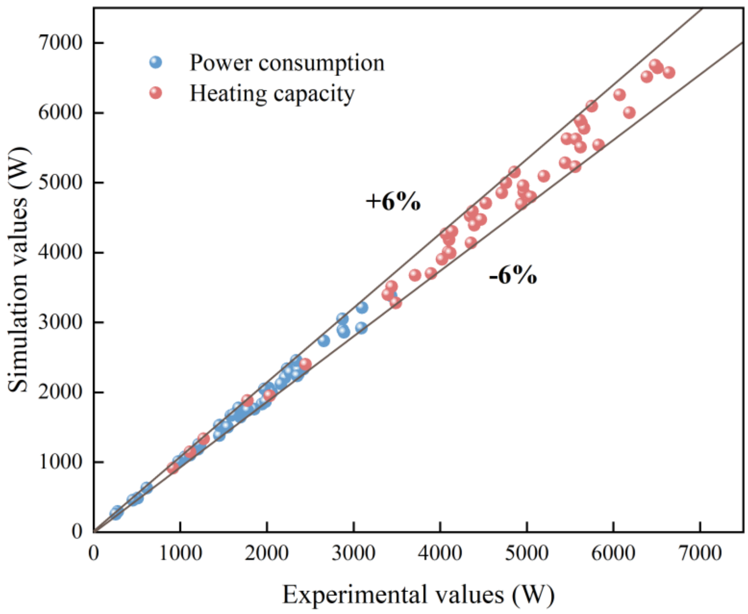

Fig.4. The validity of the TMS simulation model.

2.4 Performance evaluation

The COP is the most crucial indicator for assessing the efficiency of heat pump systems [45]. COP for a heat pump used for cabin heating is

$$COP_{cab} = \frac{\dot{Q}_{cab}}{\dot{W}_{com,cab}} = \frac{h_{dis} - h_{cab,out}}{h_{dis} - h_{suc}} \quad (4)$$

where $\dot{Q}_{cab}$ and $\dot{W}_{com,cab}$ are the cabin heating rate and compressor power consumption to heat the cabin, kW; h_{dis}, h_{suc} and $h_{c,out}$ are the enthalpy at the compressor discharge point, the enthalpy at the compress

or suction point and the enthalpy of the CO_2 fluid after heating the cabin, respectively.

COP for a heat pump used to battery heating is

$$COP_{bat} = \frac{\dot{Q}_{bat}}{\dot{W}_{com,bat}} = \frac{h_{dis} - h_{bat,out}}{h_{dis} - h_{suc}} \quad (5)$$

where $\dot{Q}_{bat}$ and $\dot{W}_{com,bat}$ are the battery heating rate and compressor power consumption to heat the battery, kW; h_{dis}, h_{suc} and $h_{bat,out}$ are the enthalpy at the compressor discharge point, the enthalpy at the compressor suction point and the enthalpy of the CO_2 fluid after heating the battery, respectively.

The percentage of CO_2 flow rate used to heat the battery is defined as,

$$k = \frac{\dot{m}_{bat}}{\dot{m}_{cab} + \dot{m}_{bat}} \quad (6)$$

The performance factor of a thermal management system is defined as,

$$COP_{TMS} = \frac{\dot{Q}_{cab} + \dot{Q}_{bat}}{\dot{W}_{com}} = \frac{\dot{m}_{cab} \cdot (h_{dis} - h_{cab,out}) + \dot{m}_{bat} \cdot (h_{dis} - h_{bat,out})}{(\dot{m}_{cab} + \dot{m}_{bat}) \cdot (h_{dis} - h_{suc})}$$

$$= (1 - k) \cdot COP_{cab} + k \cdot COP_{bat} \quad (7)$$

The COP_{TMS} is dependent on the COP_{cab} and COP_{bat} as well as the mass flow rate of the two sub-circulations, as can be seen from Eq. (7).

3 Results and discussions

3.1 Influence of coolant flow rate

Fig. 5 shows the variation of COP_{TMS} with discharge pressure for coolant flow rates ($\dot{V}_c$) from 2.23 to 8.89 L/min (Ambient temperature T_a=-20 °C, HVAC inlet air temperature $T_{air,in}$=-10 °C, chiller coolant inlet temperature $T_{c,in}$=25 °C). As can be seen, as $\dot{V}_c$ increases, the optimal COP_{TMS} decays by 19.8%, going from 2.964 to 2.378. Moreover, as $\dot{V}_c$ rises, there is a corresponding rise in the optimal P_{dis}. These phenomena find their roots in the heightened heating load placed on the battery, leading to elevated CO_2 fluid temperatures at the chiller outlet and an elevation in compressor speed. The CO_2 TMS nevertheless promises a competitive energy efficiency in spite of the challenging working circumstances at -20 °C. This is noteworthy considering the efficiency of the most used Positive Temperature Coefficient (PTC) heaters is only 0.9 [46]. Although it can be determined that the TMS has an overall optimal discharge pressure, the COP does not always increase and subsequently decrease with P_{dis} as in conventional systems (just one maximum point) [27]. To describe these causes, the optimal discharge pressures for the battery heating cycle and the cabin air heating cycle are used as benchmarks to divide the variation of COP_{TMS} with P_{dis} into three stages (as shown in Fig. 6): the first stage is before the peak COP_{cab} is reached; the second stage is after the peak COP_{cab} is reached but before the peak COP_{bat} is reached; and the third stage is after the peak COP_{bat} is reached. In addition, we define the discharge pressure that maximizes COP_{TMS} as the "global optimal discharge pressure." On the other hand, when the system does not reach its maximum COP_{TMS} at a particular discharge pressure but exhibits a trend of COP_{TMS} initially increasing and then decreasing with changes in discharge pressure around this value, we define that discharge pressure as a "local optimal discharge pressure."

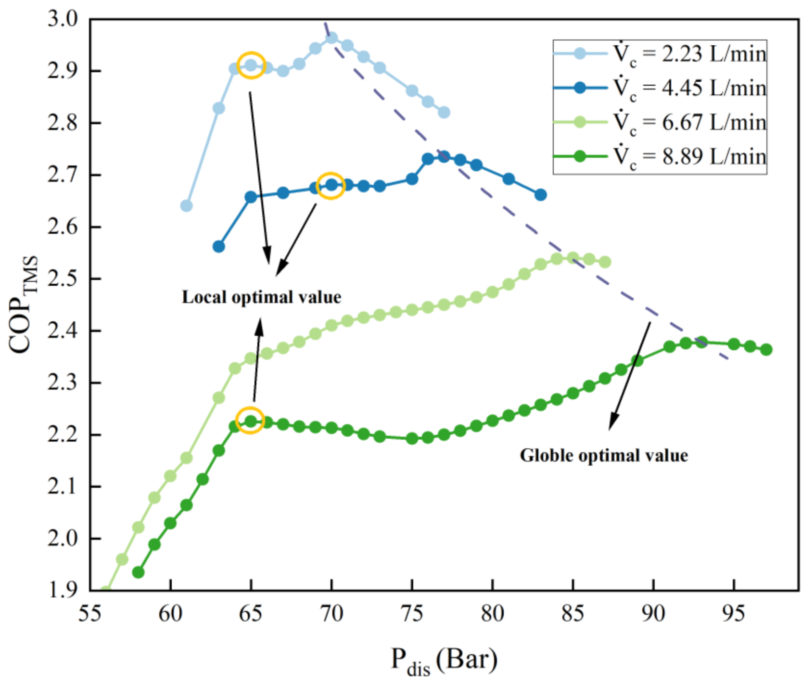

Fig.5. Variation of COP_{TMS} with P_{dis} at different $\dot{V}_c$.

Due to the limited enthalpy difference between the CO_2 chiller's outlet and inlet, the k-value in stage I is at a high level as shown in Fig.6. According to the lgP-h diagrams, the system is in a subcritical cycle during stage I, where the CO_2 condensing temperature is lower than the coolant temperature. There is a gradual increase in enthalpy difference as the P_{dis} rises because the CO_2 at the chiller outlet is superheated vapor. In addition, the rising COP_{cab} /COP_{bat} values and the relatively stable k values lead to a continuous increase in COP_{TMS}.

At stage II, the k value decreased rapidly and the decreasing trend tends to level off gradually. This is due to the rapid increase in the enthalpy difference between the chiller. The increase enthalpy difference is caused by the enhanced heat transfer coefficient in the chiller as well as the increase in the slope of the CO_2 isotherm. In addition, COP_{bat} increases with the increase of P_{dis}, and its growth rate decreases with the increase of the $\dot{V}_c$. The explanation is as follows: when $\dot{V}_c$=2.23 L/min, the chiller can ensure good heat transfer capacity in the subcritical zone, and under the near isothermal condition, the enthalpy difference rises dramatically with an increase in P_{dis}. The chiller outlet temperature rises above the CO_2 critical temperature as $\dot{V}_c$ increases. With rising temperatures, the isotherm's slope declines, which causes COP_{bat} to develop more slowly. This is clearly illustrated in the four lgP-h plots depicted in Fig. 6.

The k value is kept at a low level and tends to slowly decline in stage III. This is brought on by the gradually rising enthalpy difference in indoor HXs and chiller. Moreover, COP_{TMS} decreases when P_{dis} increases since COP_{bat} and COP_{cab} decline. In conclusion, it is evident that for COP_{TMS} to be maximized in stage II, there is at least one optimal discharge pressure value that leads to the maximum COP_{TMS}.

When $\dot{V}_c$ =2.23 L/min and $\dot{V}_c$ =4.45 L/min, the COP_{TMS} rises to the local maximum point and subsequently to the global maximum point in stage II. This can be explained by the fact that the initial value of k is at a high level, thus the rise of COP_{bat} plays a dominant role. The value of k then falls as P_{dis} rises, which causes a decline in

COP_{cab} as the main factor affecting the COP_{TMS}. Until COP_{bat} rises significantly, the COP_{TMS} global optimum is apparent. At $\dot{V}_c$= 6.67 L/min, COP_{TMS} increases and then decreases with the rise of Pdis in stage II, thus there exists only one optimal value. This is brought on by both the growing COP_{bat} and the overall greater k value. The local optimum P_{dis} occurs at the optimal value of COP_{cab} at $\dot{V}_c$=8.89 L/min. Even if k has a large value, the COP_{bat} develops very slowly, creating a local optimum point.

In general, in addition to the global optimal point, other local maximum points may still exist within stage II. The existence of a local maximum point is determined by the combination of the k value and the rising rate of COP_{bat}.

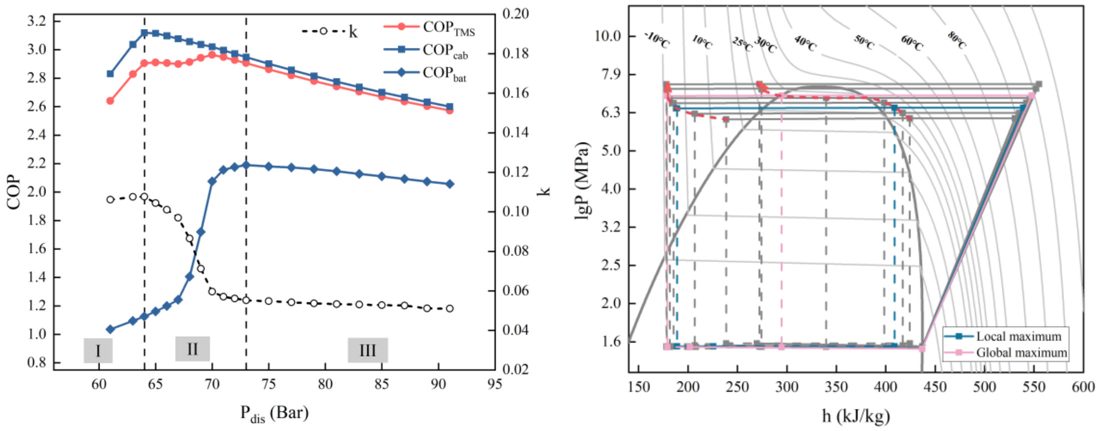

(a) $\dot{V}_c$= 2.23 L/min

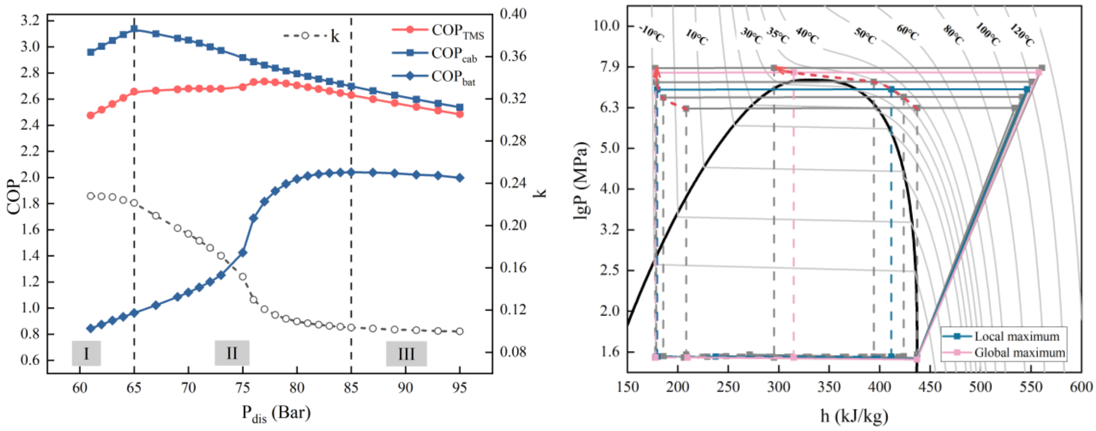

(b) $\dot{V}_c$= 4.45 L/min

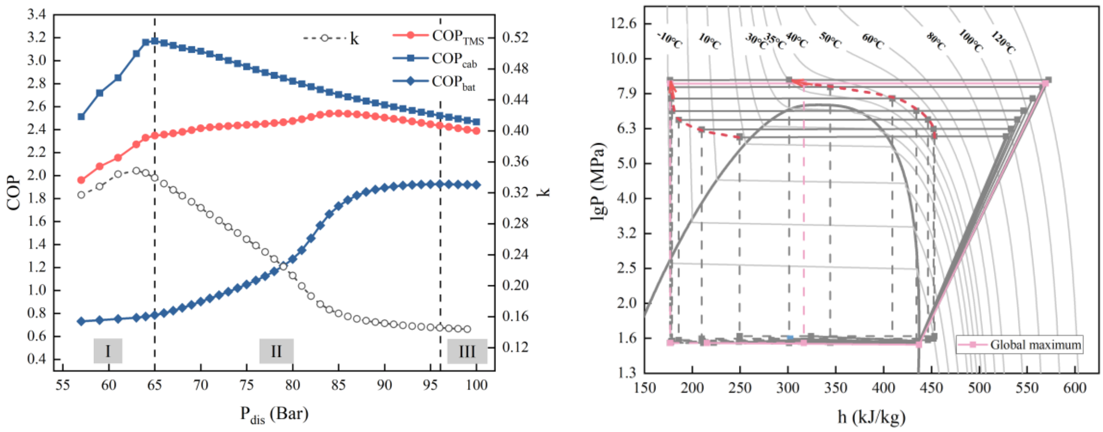

(c) $\dot{V}_c$= 6.67 L/min

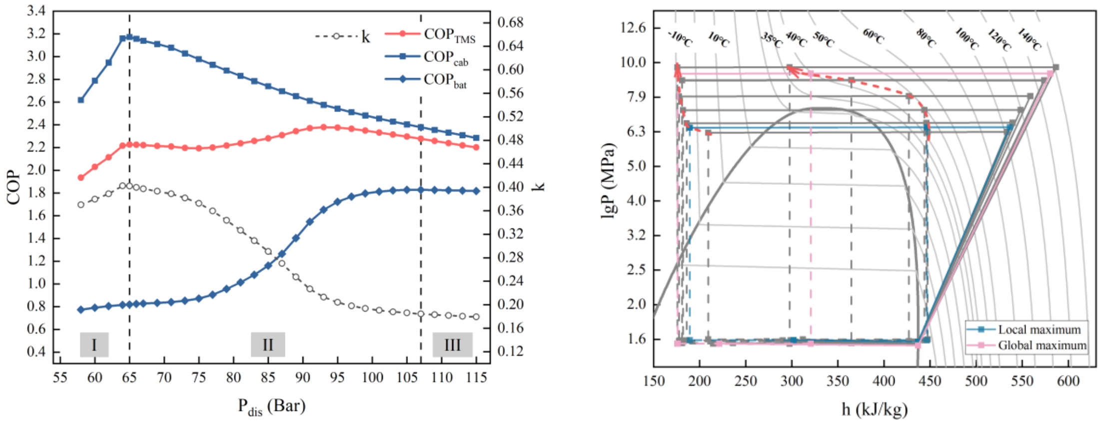

(d) $\dot{V}_c$= 8.89 L/min

Fig.6. Trends of COP_{TMS}, COP_{cab}, COP_{bat} and k at different stages as well as lgP-h diagrams.

3.2 Influence of chiller inlet coolant temperature

Fig. 7 shows the variation of the COP_{TMS} with P_{dis} for T_a=-20 °C and $T_{air,in}$=-10 °C. It can be seen the optimal P_{dis} increases from 87 to 97 Bar as chiller inlet coolant temperature ($T_{c,in}$) increases from 20 °C to 30 °C at $\dot{V}_c$=8.89 L/min, but the $COP_{TMS,opt}$ decreases from 2.500 to 2.277, a 8.9% reduction. This is due to the increase in the chiller outlet CO_2 temperature and the high k value. At $\dot{V}_c$=8.89 L/min, the local optimum P_{dis} exists at the optimal value of 65 Bar as $T_{c,in}$ increases from 20 °C to 30 °C, which is also the optimal value of COP_{cab}. However, At $\dot{V}_c$=4.45 L/min, the optimal P_{dis} increases and then decreases with the increase of $T_{c,in}$. This is due to a slower

COP_{bat} increase in the stage II caused by the high CO_2 temperature at the chiller outlet (as shown in Fig. 8). At $T_{c,in}$=30 °C, the $P_{pse\text{-}opt}$ value is 71 Bar and the maximum COP_{TMS} is 2.614, while the local optimal discharge pressure value is 83 Bar and the local maximum COP_{TMS} is 2.589. The global optimum COP_{TMS} is only 0.97% higher than the local optimum value.

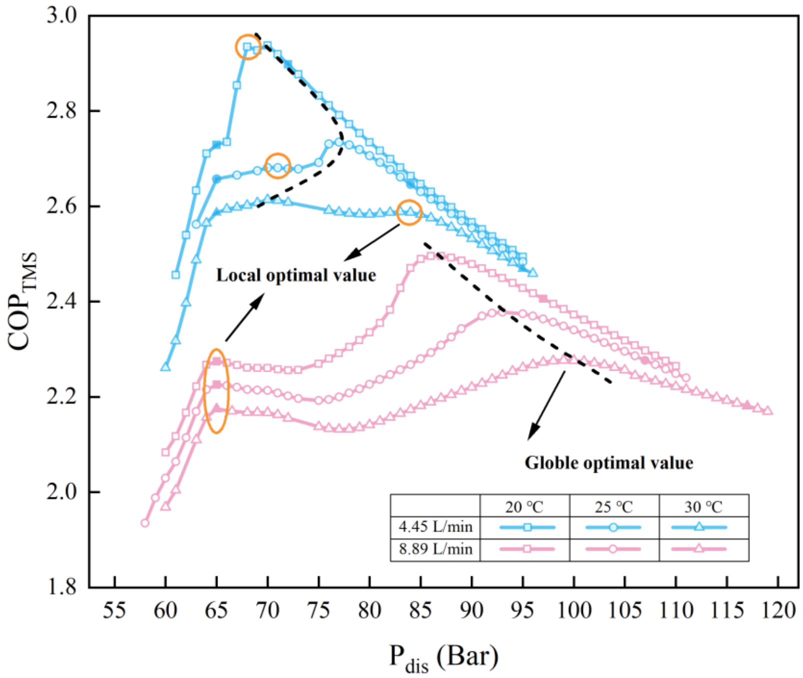

Fig.7. Variation of COP_{TMS} with P_{dis} at different $T_{c,in}$.

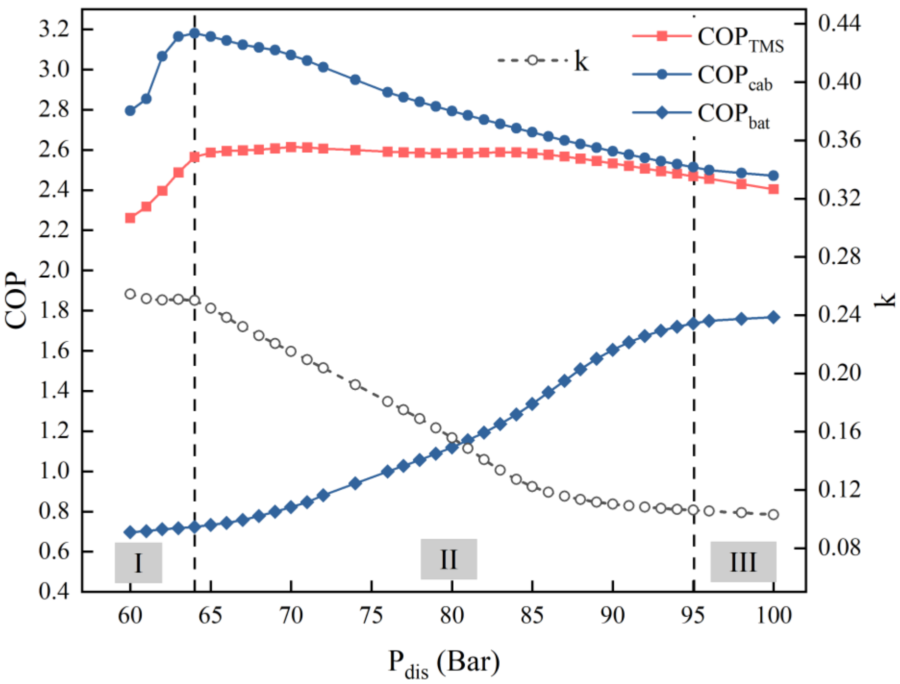

Fig.8. Trends of COP_{TMS}, COP_{cab}, COP_{bat} and k at different stages ($\dot{V}_c$=4.45 L/min, $T_{c,in}$=30 °C)

3.3 Influence of HVAC inlet air temperature

Fig. 9 depicts the variation of COP_{TMS} concerning P_{dis} for HVAC inlet air temperatures ($T_{air,in}$) ranging from -10°C to 20°C. It is evident that the parameter k increases proportionally with the elevation of $T_{air,in}$. This phenomenon can be attributed to the reduction in heating demands within the cabin. Furthermore, there is a noteworthy decrease in the maximum COP_{TMS} value, dropping from 2.735 to 2.302, representing a substantial 15.8% reduction as $T_{air,in}$ increases from -10°C to 20°C. This reduction can be attributed to the fact that, despite the increased heating load required when $T_{air,in}$ is -10°C, the system experiences enhanced efficiency due to the lower CO_2 outlet temperature from the indoor HXs. Besides, a local optimum P_{dis} exists only at inlet air temperature of -10 °C, which is due to the small k values.

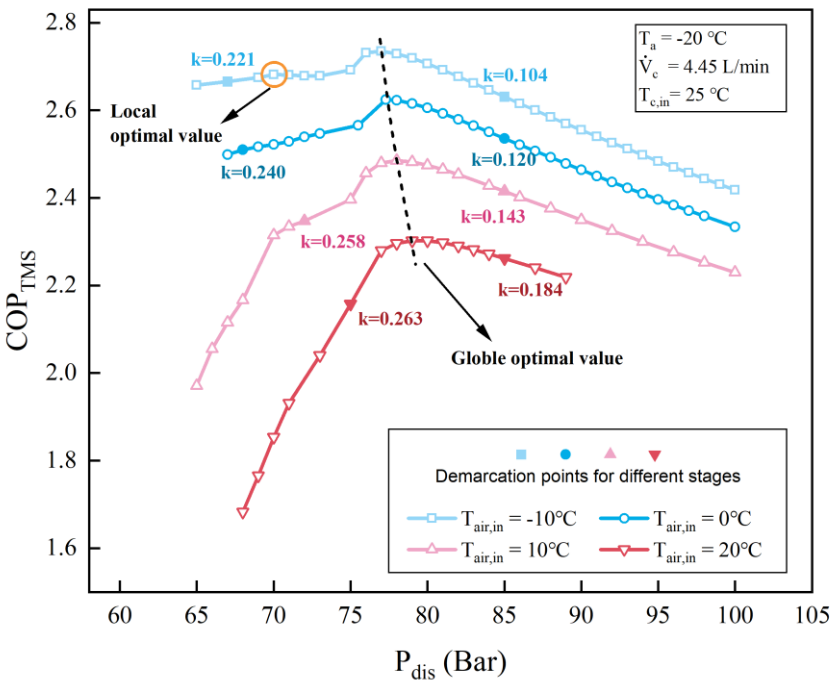

Fig.9. Variation of COP_{TMS} at different $T_{air,in}$.

Fig.10. shows the values of $COP_{TMS,opt}$ and $P_{dis,opt}$ for $T_{air,\ in}$ increases from -10 °C to 20 °C (T_a=-20 °C, $T_{c,in}$=25 °C, $\dot{V}_c$=2.23 L/min~8.89 L/min). Contrary to the typical heat pump system for cabin heating, there have little effect of $T_{air,in}$ on the optimal discharge pressure, with a 3~5 bar change from -10 °C to 20 °C. However, as $\dot{V}_c$ increases from 2.23 L/min to 8.89 L/min, there is a corresponding increase in $P_{dis,opt}$ by approximately 22 to 24 bar. Therefore, it becomes evident that $\dot{V}_c$ exerts a more pronounced influence on the global optimal discharge pressure than $T_{air,in}$. This phenomenon arises due to the fact that the CO_2 fluid temperature at the chiller outlet is higher than that at the indoor heat exchanger outlet. This results in a steeper slope of the isotherms on one hand and, on the other hand, when COP_{TMS} reaches its optimum value, the indoor HXs' heat transfer capacity is already approaching its optimal state, while the chiller's heat transfer capacity increases rapidly with an increase in discharge pressure. Conversely, $T_{air,in}$ exhibits a more significant effect on COP_{TMS}, especially in scenarios where $\dot{V}_c$=2.23 L/min. This is primarily attributed to the fact that the heating load predominantly originates from the cabin. When $T_{air,in}$ is -10°C, COP_{TMS} experiences an increase of 16.29% to 24.21% compared to the case where $T_{air,in}$ is 20°C.

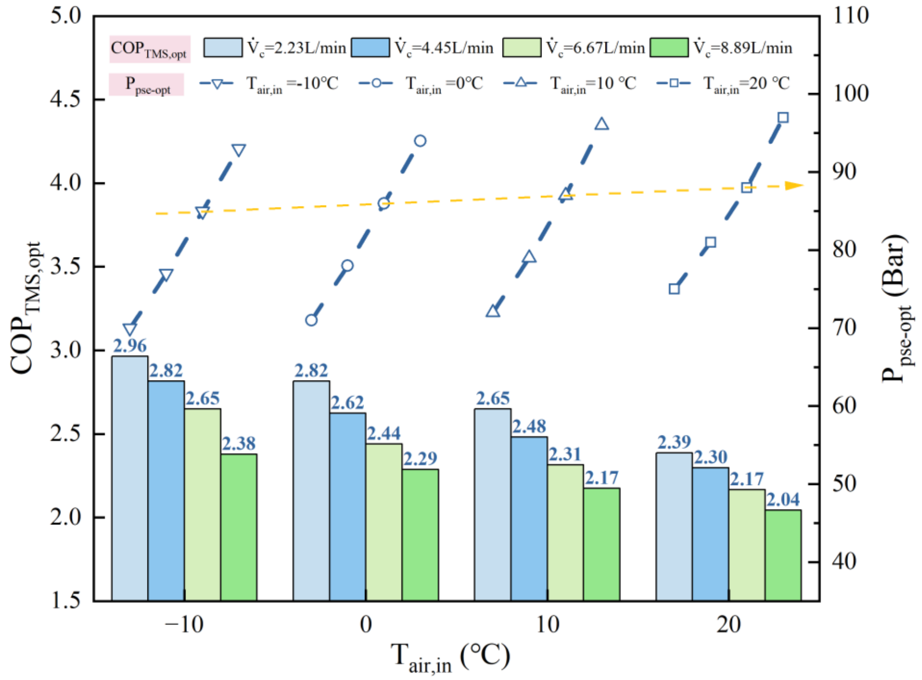

Fig.10. $COP_{TMS,opt}$ and $P_{dis,opt}$ values in different $T_{air,in}$.

3.4 Influence of ambient temperature

According to Fig. 11, when the ambient temperature rose from -20 °C to 0 °C, the global optimal discharge pressure only increased by 2~8 Bar at constant $\dot{V}_c$ ($T_{air,in}$=0 ℃, $T_{c,in}$=25 ℃). In contrast, $\dot{V}_c$ increases from 2.23 L/min to 8.89 L/min, the global optimal discharge pressure increases by 23~29 Bar at the same T_a. Thus $\dot{V}_c$ has a greater effect on the optimal P_{dis} compared to the ambient temperature. However, the ambient temperature has a significant effect on the $COP_{TMS,opt}$ values. In addition, the optimal k value increases with the increase of T_a, which is caused by the decrease of cabin heating load.

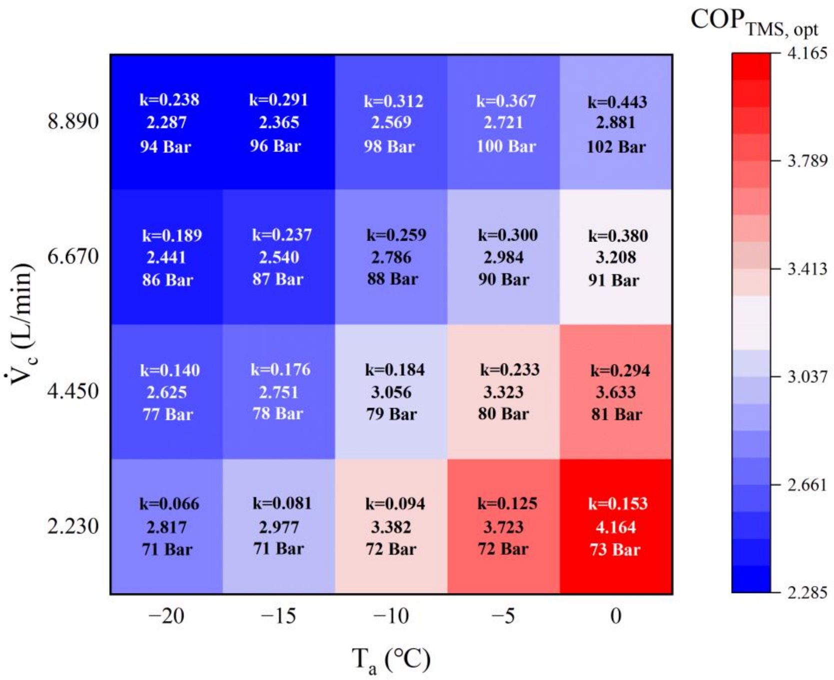

Fig.11. $COP_{TMS,\ opt}$ and $P_{dis,\ opt}$ values in different T_a.

In summary, there must be an optimal exhaust pressure for the cabin-and-battery mixed heating mode to maximize the COP_{TMS}, which is determined by both the heat transfer capacity limit and the isotherm slope, regardless of the system state of subcritical or transcritical cycles. Therefore, the discharge pressure that maximizes the COP_{TMS} can be referred to as the pseudo-optimal discharge pressure ($P_{pse\text{-}opt}$). In an EV with a cabin volume of 3.5 m^3, coolant flow rate $\dot{V}_c$, chiller inlet coolant temperature $T_{c,in}$, HVAC inlet air temperature $T_{air,in}$ and ambient temperature T_a are all factors that affect the $P_{pse\text{-}opt}$. Among them, $\dot{V}_c$ and $T_{c,in}$ are more important influencing factors. In this study, a predictive equation (Eq. (8)) for $P_{pse\text{-}opt}$ was obtained using Response Surface Analysis [47]. As can be seen from Fig. 12, the prediction deviation is within 5%.

$$P_{pse-opt} = T_a\left(-0.0234T_a + 0.0545T_{c,in} - 1.6643\right) + 1.9356T_{c,in} + 3.7113\dot{V}_c$$
$$+T_{air,in}\left(-0.0402T_{c,in} - 0.0288\dot{V}_c + 1.3986\right) + 14.5906 \quad (8)$$

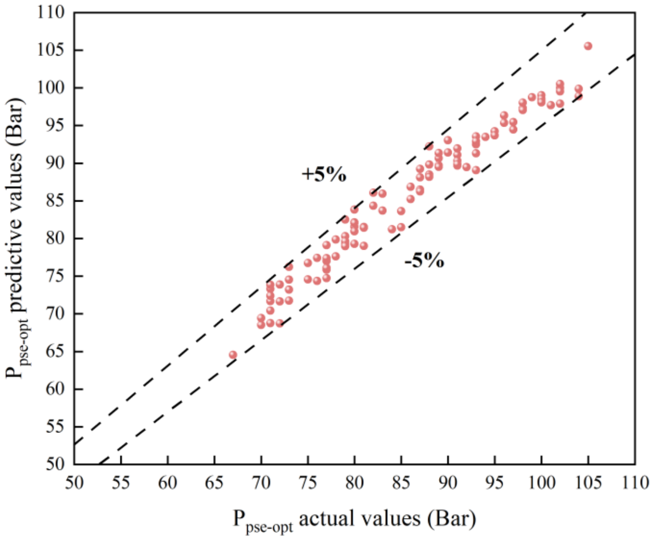

Fig.12. Comparison of actual values and calculated values.

Conclusion

This paper investigates the system characteristics of the CO_2 thermal management system in cabin-and-battery mixed heating mode in winter. We built a liquid-cooled CO_2 TMS test rig and corresponding simulation model. Additionally, numerous PI controllers and a cabin thermal model were combined to fully analyze the winter performance of the CO_2 liquid-cooled TMS. The main conclusions are as follows:

(1) The optimal discharge pressures for the battery heating cycle and the cabin air heating cycle are used as benchmarks to divide the variation of COP_{TMS} with P_{dis} into three stages. There is a pseudo-optimal discharge pressure to maximize the COP_{TMS} in stage II regardless of the system state of subcritical or transcritical cycles.

(2) In addition to the $P_{pse\text{-}opt}$, other local maximum points may still exist within stage II. The existence of a local maximum point is determined by the combination of the k value and the rising rate of COP_{bat}.

(3) When T_a=-20 °C, $T_{c,in}$=30 °C, $\dot{V}_c$=8.89 L/min and $T_{air,in}$=-10 °C, the $COP_{TMS,opt}$ is 2.277, which significantly outperforms the conventional PTC heaters with an efficiency as low as 0.9. This comparison solidifies the proof that the CO_2 TMS demonstrates a competitive energy efficiency despite the demanding operational

conditions.

(4) The $P_{pse\text{-}opt}$ increases with the increase of $T_{air,in}$, T_a and $\dot{V}_c$. However, the variation pattern of $P_{pse\text{-}opt}$ with $T_{c,in}$ varies under different battery heating loads. A $P_{pse\text{-}opt}$ prediction equation is proposed for maximizing the performance of CO_2 thermal management system in cabin-and-battery mixed heating mode for winter. It presents a solution for the optimal control of the CO_2 thermal management system.

Acknowledgments

The corresponding author is grateful to the Foundation for Innovative Research Groups of the National Natural Science Foundation of China (No.51721004), the National Natural Science Foundations of China (No.52006161) and China Scholarship Council (No. 202206280214).

References

[1] G. Xia, L. Cao, G. Bi, A review on battery thermal management in electric vehicle application, Journal of Power Sources, 2017, 367, 90-105.

[2] P. V. Chombo, Y. Laoonual, A review of safety strategies of a Li-ion battery, Journal of Power Sources, 2020, 478, 228649.

[3] Y. Wang, J. Wu, Thermal performance predictions for an HFE-7000 direct flow boiling cooled battery thermal management system for electric vehicles, Energy Conversion and Management, 2020, 207, 112569.

[4] Q. Wang, B. Jiang, B. Li, Y. Yan, A critical review of thermal management models and solutions of lithium-ion batteries for the development of pure electric vehicles, Renewable and Sustainable Energy Reviews, 2016, 64, 106-128.

[5] W. Ca, C. Zhao, Y. Wang, T. Dong, F. Jiang, Thermal modeling of full-size-scale cylindrical battery pack cooled by channeled liquid flow, International Journal of Heat and Mass Transfer, 2019, 138, 1178-1187.

[6] Y. Fan, Z. Wang, T. Fu, H. Wu, Numerical investigation on lithium-ion battery thermal management utilizing a novel tree-like channel liquid cooling plate exchanger,

International Journal of Heat and Mass Transfer, 2022, 183, Part B, 122143.
[7] Z. An, C. Zhang, Y. Luo, J. Zhang, Cooling and preheating behavior of compact power Lithium-ion battery thermal management system, Applied Thermal Engineering, 2023, 226, 120238.
[8] A. Alahmer, A. Mayyas, A. A. Mayyas, M.A. Omar b, D. Shan, Vehicular thermal comfort models; a comprehensive review, Applied Thermal Engineering, 2011, 31(6–7), 995-1002.
[9] J. H. Ahn, J. S. Lee, C. Baek, Y. Kim, Performance improvement of a dehumidifying heat pump using an additional waste heat source in electric vehicles with low occupancy, Energy, 2016, 115(15) ,67-75.
[10] M. H. Park, S. C. Kim, Heating Performance Characteristics of High-Voltage PTC Heater for an Electric Vehicle, Energies, 2017, 10(10), 1494.
[11] S. H. Hong, D. S. Jang, S. Yun, Jae H. Baek, Y. Kim, Performance improvement of heat pumps using novel microchannel heat exchangers with plain-louver fins during periodic frosting and defrosting cycles in electric vehicles, Energy Conversion and Management, 2020, 223, 113306.
[12] H. Wang, F. Cao, F. Jia, Y. Song, X. Yin, Potential assessment of transcritical CO_2 secondary loop heat pump for electric vehicles, Applied Thermal Engineering, 2023, 224, 119921.
[13] M. Hosoz, M. Direk, Performance evaluation of an integrated automotive air conditioning and heat pump system, Energy Conversion and Management, 2006, 47 (5), 545-559.
[14] K. Zhang, M. Li, C. Yang, Z. Shao, L. Wang, Exergy Analysis of Electric Vehicle Heat Pump Air Conditioning System with Battery Thermal Management System, Journal of Thermal Science, 2020, 29, 408–422.
[15] J. Cen, Z. Li, F. Jiang, Experimental investigation on using the electric vehicle air conditioning system for lithium-ion battery thermal management, Energy for Sustainable Development, 2018, 45, 88-95.
[16] S. Park, D.S. Jang, D.C. Lee, S. H. Hong, Y. Kim, Simulation on cooling

performance characteristics of a refrigerant-cooled active thermal management system for lithium-ion batteries, International Journal of Heat and Mass Transfer, 2019, 135, 131-141.

[17] J. Cen, F. Jiang, Li-ion power battery temperature control by a battery thermal management and vehicle cabin air conditioning integrated system, Energy for Sustainable Development, 2020, 57, 141-148.

[18] X. Tang, Q. Guo, M. Li, C. Wei, Z. Pan, Y. Wang, Performance analysis on liquid-cooled battery thermal management for electric vehicles based on machine learning, Journal of Power Sources, 2021, 494, 229727.

[19] M. Shen, Q. Gao. System simulation on refrigerant-based battery thermal management technology for electric vehicles, Energy Conversion and Management, 2020, 203, 112176.

[20] Z. Tian, W. Gan a, X. Zhang, B. Gu, L. Yang, Investigation on an integrated thermal management system with battery cooling and motor waste heat recovery for electric vehicle, Applied Thermal Engineering, 2018, 136, 16-27.

[21] J. Guo, F. Jiang, A novel electric vehicle thermal management system based on cooling and heating of batteries by refrigerant, Energy Conversion and Management, 2021, 237, 114145.

[22] UNIDO. The Montreal protocol evolves to fight climate change, 2016.

[23] H. Wang, Y. Song, Y. Qiao, S. Li, F. Cao, Rational assessment and selection of air source heat pump system operating with CO_2 and R407C for electric bus, Renewable Energy, 2022, 182, 86-101.

[24] J. Dong, Y. Wang, S. Jia, X. Zhang, L. Huang, Experimental study of R744 heat pump system for electric vehicle application, Applied Thermal Engineering, 2021, 183, 116191.

[25] D. Wang, B. Yu, W. Li, J. Shi, J. Chen, Heating performance evaluation of a CO_2 heat pump system for an electrical vehicle at cold ambient temperatures, Applied Thermal Engineering, 2018, 142, 656-664.

[26] S.M. Liao, T.S. Zhao, A. Jakobsen, A correlation of optimal heat rejection

pressures in transcritical carbon dioxide cycles, Applied Thermal Engineering, 2000, 20(9), 831-841.

[27] A. Wang, F. Cao, X. Yin, F. Jia, J. Fang, X. Wang, Pseudo-optimal discharge pressure analysis of transcritical CO_2 electric vehicle heat pumps due to temperature glide, Applied Thermal Engineering, 2022, 215, 118856.

[28] X. Yin, J. Fang, A. Wang, Y. Song, F. Cao, X. Wang, A novel CO_2 thermal management system with battery two-phase (evaporative) cooling for electric vehicles, Results in Engineering, Volume 16, December 2022, 100735.

[29] A. Wang, X. Yin, Z. Xin, F. Cao, Z. Wu, B. Sundén, D. Xiao, Performance optimization of electric vehicle battery thermal management based on the transcritical CO_2 system, Energy, Volume 266, 1 March 2023, 126455

[30] H. Wang, W. Wang, Y. Song, X. Yang, P. Valdiserri, E. Rossi di Schio, G. Yu, F. Cao, Data-driven model predictive control of transcritical CO2 systems for cabin thermal management in cooling mode, Applied Thermal Engineering, 2023, 235, 25 121337.

[31] X. Li, H. Tian, G. Shu, M. Zhao, C. N. Markides, C. Hu, a Potential of carbon dioxide transcritical power cycle waste-heat recovery systems for heavy-duty truck engines, Applied Energy, 2019, 250, 15,1581-1599.

[32] R. Zhao, H. Zhang, S. Song, F. Yang, X. Hou, Y. Yang, Global optimization of the diesel engine–organic Rankine cycle (ORC) combined system based on particle swarm optimizer (PSO), Energy Conversion and Management, 2018, 174 (15), 248-259.

[33] M. N. Nabi, B. Ray, F. Rashid, W. A. Hussam, S.M. M, Parametric analysis and prediction of energy consumption of electric vehicles using machine learning, Journal of Energy Storage, 2023, 72, Part B, 20, 108226.

[34] F. W. Dittus, L. M. K. Boelter, Heat transfer in automobile radiators of the tubular type, University of California Publications of Engineering, 1930, 2, 443-61.

[35] L. Tang, M. M. Ohadi, A.T. Johnson, Flow Condensation in Smooth and Micro-fin Tubes with HCFC-22, HFC-134a and HFC-410A Refrigerants. Journal of Enhanced Heat Transfer, 2000, 7, 289-326.

[36] K. E. Gungor, R. H. S. Winterton, Simplified general correlation for saturated flow boiling and comparisons of correlations with data, Chemical engineering research & design, 1987, 65(2), 148-156.

[37] S. H. Yoon, J. H. Kim, Y. W. Hwang, M. S. Kim, K. Min, Y. Kim, Heat transfer and pressure drop characteristics during the in-tube cooling process of carbon dioxide in the supercritical region, International Journal of Refrigeration, 2003, 26, 857–864.

[38] Y. J. Chang, C. C. Wang, A generalized heat transfer correlation for louver fin geometry, Heat Mass Transfer, 1997, 40, 533-544.

[39] D. A. Cruz, P. M. Coelho, M. A. Alves, A simplified method for calculating heat transfer coefficients and friction factors in laminar pipe flow of non-newtonian fluids, Journal of Heat Transfer, 2012, 134.

[40] K. T. Trinh, The wall shear rate in non-Newtonian turbulent pipe flow, Physics, 2010.

[41] B.D. Rasmussen, A. Jakobsen, Review of Compressor Models and Performance Characterizing Variables, in: International Compressor Engineering Conference, 2000, paper 1429.

[42] B. Munson, D. Young, Fundamentals of Fluid Mechanics, 4th Edition, John Wiley and Sons, Inc., New York, 2002.

[43] S. Sisavath, X. Jing, C. C. Pain, R. W. Zimmerman, Creeping Flow Through an Axisymmetric Sudden Contraction or Expansion, Jorunal of Fluids Engineering, 2002, 124(1): 273-278.

[44] S.J. Kline, F.A. Mcclintock, Describing Uncertainties in Single-Sample Experiments, Mechanical engineering, 1953, 75, 3-9

[45] American Society of Heating, Refrigerating and Air-Conditioning Engineers (ASHRAE), 2009.

[46] J. Wu, G. Zhou, M. Wang, A comprehensive assessment of refrigerants for cabin heating and cooling on electric vehicles, Applied Thermal Engineering, 2020, 174, 115258.

[47] M. A. Bezerra, R. E. Santelli, E. P. Oliveira, L. S. Villar, L. A. Escaleira, Response

surface methodology (RSM) as a tool for optimization in analytical chemistry, Talanta, 2008, 76, Issue 5, 965-977.